Chapter-5

Erosion Behavior of Fe-18Cr-21Mn-0.65N Austenitic Stainless Steel

5.1 Introduction

Solid particle erosion (SPE) is a form of surface damage caused by the impact of hard fine particles on the surface of the material with sufficient velocity for appreciable time [120]. This phenomenon reduces service life of the material. It can occur in many cases such as in transport pipes, turbine blades, heat exchangers, power generation units, etc. [121]. In hydroelectricity generation, underwater parts operating in silt ladens suffer metal erosion and it causes serious problems such as failure of components, plant shut down, heavy loss in power generation, etc. [77, 122]. Erosion is a serious problem in mining and waste disposal industry. In gas pipeline industry, flowing gas containing solid particles causes erosion on internal wall of valves. Similarly in steam reforming units where natural gas or solid carbonaceous feedstock such as coal, coke, biomass, etc. is reformed into syngas ($CO+H_2$) with other gases, carrying sand particles also causes solid particle erosion of components [123, 124]. Solid particle erosion (SPE) mainly depends on the type of particle, its size and shape, angle of impact, and velocity of impact as described in Chapter 2. Another important factor is service temperature which increases the severity of SPE due to the synergistic effect of high temperature oxidation and erosion. Traditionally, materials having a good combination of mechanical properties such as martensitic, austenitic stainless steels and Ni based superalloys are used in such industries [125]. Nitrogen is a better solid solution strengthener than carbon, it improves corrosion resistance and most importantly reduces the cost by replacing nickel [126]. A study by AK Chauhan et al. [77] on solid particle erosion of 13/4 martensitic stainless steel and of nitrogen alloyed nitronic stainless steel (23wt% Cr, 4wt% Ni, and 0.38wt% N) shows high resistance towards solid particle erosion of nitronic stainless steel due to high hardness and ductility, attributed to uniform distribution of hard carbides in the austenitic matrix. In most of the industrial applications stainless steel components are simultaneously exposed to oxidation and erosion. As shown in the Chapter 3, the high manganese low nickel austenitic stainless steel

provides better oxidation resistance at higher temperatures by forming a uniform and intact oxide layer. Likewise, this chapter presents erosion behavior of pre oxidized nickel free nitrogen stabilized austenitic stainless steel (Fe-18Cr-21Mn-0.65N) in air at four different temperatures. The specimens were first oxidized in air for 100 h at 400, 500, 600 and 700°C and then subsequently subjected to solid particle erosion at 400, 500, 600 and 700°C respectively, with particle velocity of 100 m/s. The erodent discharge rate was maintained at 4.6±0.5 gm/min and three impact angle 60°, 75°, and 90° were employed. Optical microscopy, Scanning Electron Microscopy (SEM) and X-ray Diffraction technique (XRD) were used to characterize the eroded surface. Tensile tests and microhardness measurements were performed to better understand the erosion behavior. Erosion rate increased steadily up to 500°C, however, there was an exponential increase at 600 and 700°C. It is found to be associated with a decrease in tensile strength and hardness of the steel. High temperature oxidation (pre-exposure) resulted in precipitation of harmful chromium nitride (Cr_2N) which accelerated the erosion rate at 600 and 700°C. The main mechanisms of erosion were ploughing, indenting, delamination and pitting and varied with pre-exposure and test conditions.

5.2. Results

5.2.1 Weight Loss Analysis

Figure 5.1 (a-e) shows the weight loss vs time plot of the samples, solution treated and exposed at different temperatures from 400 to 700°C for 100 h, eroded at respective temperatures of exposure from RT to 700°C at impact angles of 60°, 75° and 90°. At room temperature (**Figure 5.1 a**) weight loss was minimum and was lowest at normal angle whereas at 700°C (**Figure 5.1 e**) weight loss was highest at an impact angle of 60° and was lower at the normal angle. **Table 5.1** presents the values of erosion rate at different temperatures with varying angles.
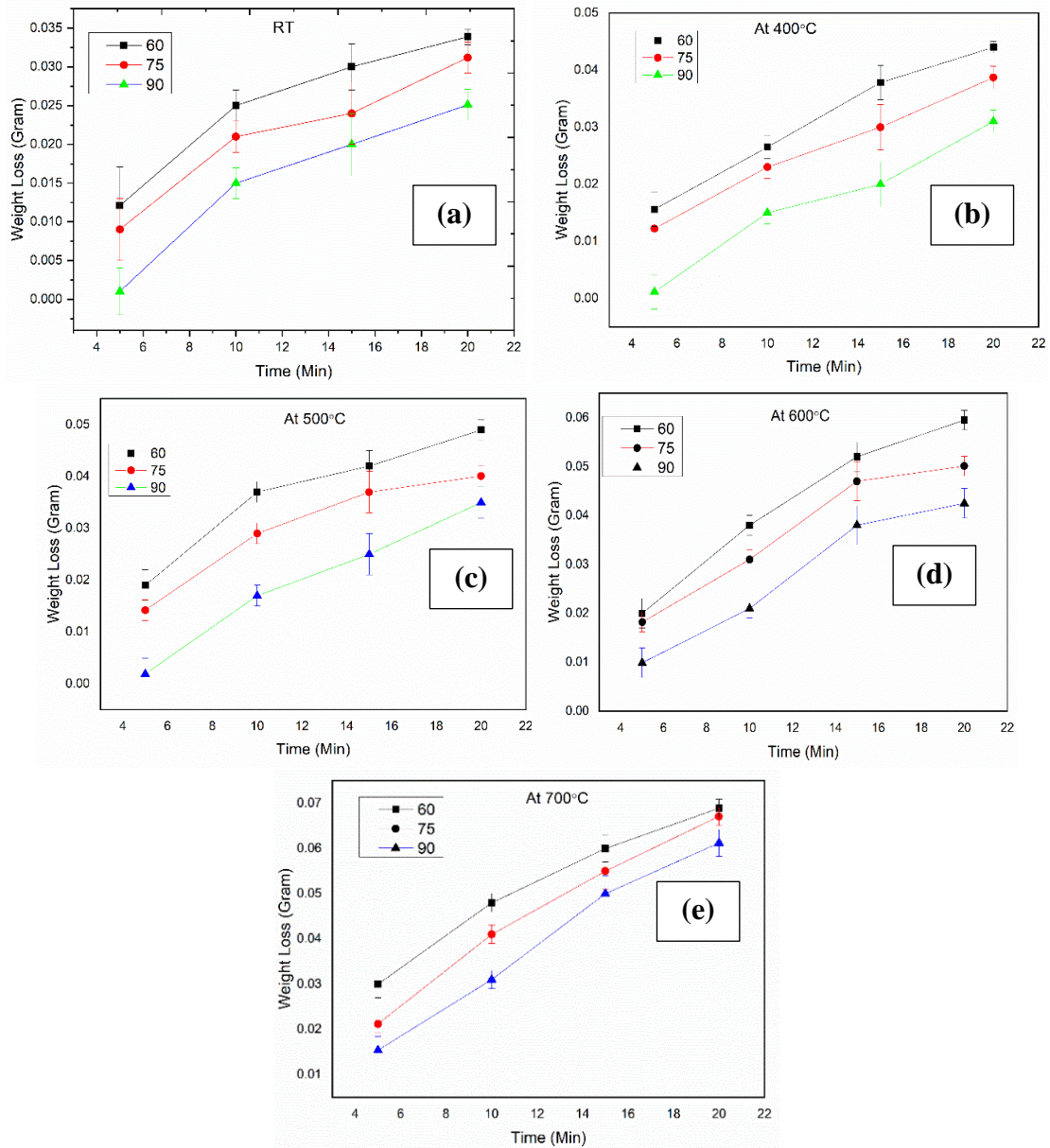
Figure 5.1: Weight loss vs time plots of Fe-18Cr-21Mn-0.65N austenitic stainless steel eroded at (a) RT, (b) 400°C, (c) 500°C, (d) 600°C and (e) 700°C at three impact angles of 60°, 75° and 90°, solution treated, pre-exposed at respective temperatures of erosion, from RT to 700°C.

Table 5.1. Erosion rate (ER) at different impact angles and temperatures.

Angle	ER (g/g) RT $\times 10^{-4}$	error $\times 10^{-5}$ ±	ER(g/g) 400°C $\times 10^{-4}$	error $\times 10^{-5}$ ±	ER(g/g) 500°C $\times 10^{-4}$	error $\times 10^{-5}$ ±	ER(g/g) 600°C $\times 10^{-4}$	error $\times 10^{-5}$ ±	ER(g/g) 700°C $\times 10^{-4}$	error $\times 10^{-5}$ ±
60°	3.76	1.01	4.88	1.50	5.44	1.12	6.61	1.34	7.65	1.32
75°	3.46	1.50	4.30	1.23	4.45	1.22	5.56	1.40	7.45	1.01
90°	2.78	1.02	3.44	1.30	3.88	1.11	4.72	1.23	6.80	1.22

5.2.2 Erosion rate

Figure 5.2a shows erosion rate vs temperature plot. It can be seen that at lowest impingement angle of 60˚ erosion rate was highest and at the highest angle of 90˚ was lowest, and at 75˚ of impingement erosion rate was between these two. The weight loss at all impact angles increased rapidly above 600℃, while at RT, 400 and 500℃, weight loss was comparatively less. Erosion rate increased steadily up to 500℃, however, the increase in erosion rate was exponential at 600 and 700℃. **Figure 5.2 b** shows erosion rate at different temperatures. The difference between the erosion rate at different angles was less at 25℃ (RT) and a similar trend was observed also at 700℃. However, at 400, 500, and 600℃ the difference in erosion rate at the lower and higher impingement angles was more and the dependence of erosion rate on the angel of impingement increased.
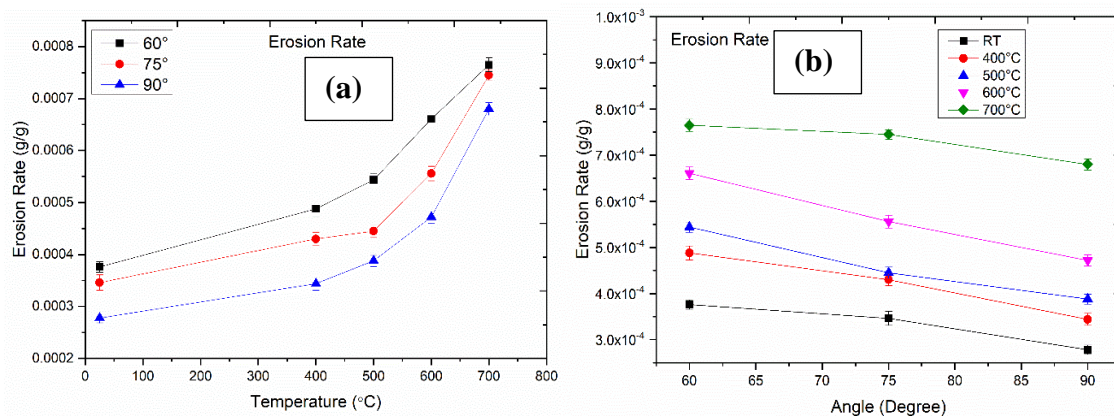

Figure 5.2: Plots showing erosion behavior of the Fe-18Cr-21Mn-0.65N austenitic stainless steel: (a) erosion rate vs temperature, (b) erosion rate vs angle of impact.

5.2.3 Hardness Profile

It is important to mention here that hardness of the samples, pre exposed at different temperatures from 400 to 700℃ and eroded at the respective temperatures was measured at room temperature. **Figure 5.3 (a-e)** shows variation of hardness on the cross section, in the scar area, with depth. It shows that at all the test temperatures of erosion of the pre-exposed samples at the respective test temperature and different angles of impingement, there was an increase in hardness in the surface region. The bulk hardness of the eroded

specimens was measured at higher applied load of 10 Newton, at center of the cross section

of the eroded specimens and was found to be lower compared to that in the surface region,
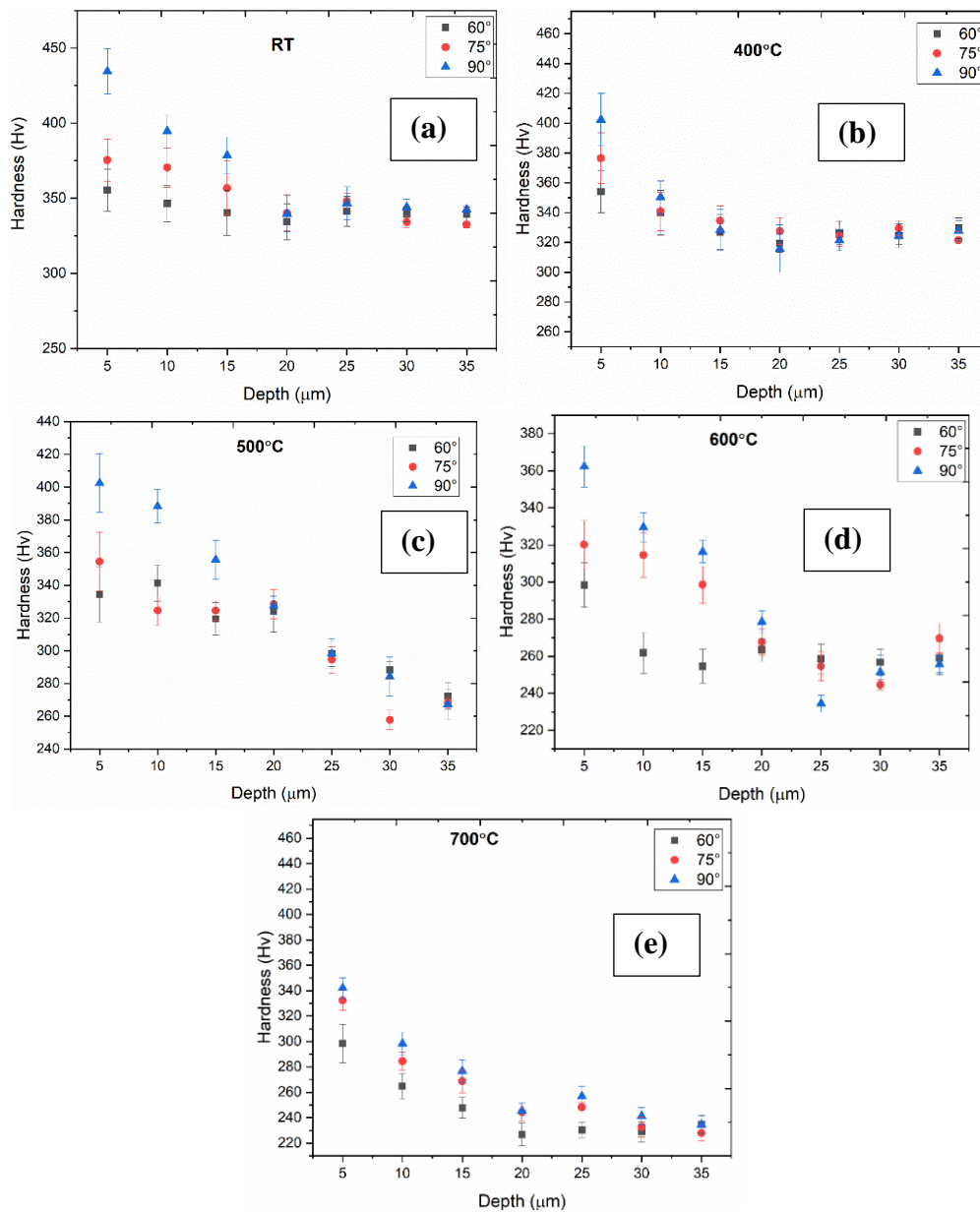
in all the conditions (Table 5.3).

Figure 5.3: Microhardness vs depth plot of Fe-18Cr-21Mn-0.65N austenitic stainless steel eroded at (a) room temperature, (b) 400°C, (c) 500°C, (d) 600°C and (e) 700°C.

The hardness of the eroded solution treated specimen, close to surface (at 5µm depth) was

highest (434 Hv) at 90° impingement whereas that of the specimen pre exposed as well as

eroded at 700°C was lowest (362 Hv). It could be due to oxidation in the surface region and

also due to precipitation of harmful nitrites, from the exposure at higher temperatures [127].

Hardness at the surface was higher compared to that in the bulk, especially of the specimens impinged at 90°, pre exposed at all the temperatures for 100 h. Surface hardness of the specimens impinged at 90°was substantially higher than of those impinged at 60° and 75°. This increase in hardness is attributed to surface deformation at 90° of impingement.

5.2.4 Tensile Behavior

Figure 5.4 a shows engineering stress strain plots of the Fe-18Cr-21Mn-0.65N austenitic stainless steel, solution treated and pre-exposed from 400 -700°C for 100 h, and tested at the respective temperature of the pre-exposure. It shows that the yield strength at 400, 500 and 600°C was not much affected by the 100 h of exposure at these temperatures. Tensile strength of the sample pre-exposed at 600 and 700°C was decreased by 7% and 13% respectively while there was only a marginal change in the tensile strength of the solution treated specimens and pre-exposed at 400, 500°C and tested at respective temperature of pre-exposure.

There was a decrease of 21% and 29% in ductility (elongation) of the specimens   pre-exposed at 600 and 700°C respectively and tested at the respective temperature; however, the drop in ductility of the specimens pre-exposed at 400°C and 500°C was comparably less. This drop in tensile properties can be attributed to precipitation of chromium nitrides resulting in decrease in the solid solution strengthening. Table 5.2 shows the yield strength, tensile strength, and % elongation of the specimens pre-exposed at different temperatures and tested at the respective temperature. **Figure 5.4 b** shows the true stress and true strain behavior of high manganese nitrogen stabilized austenitic stainless steel. Table 5.4 shows that the work hardening coefficient decreased with an increase in temperature.
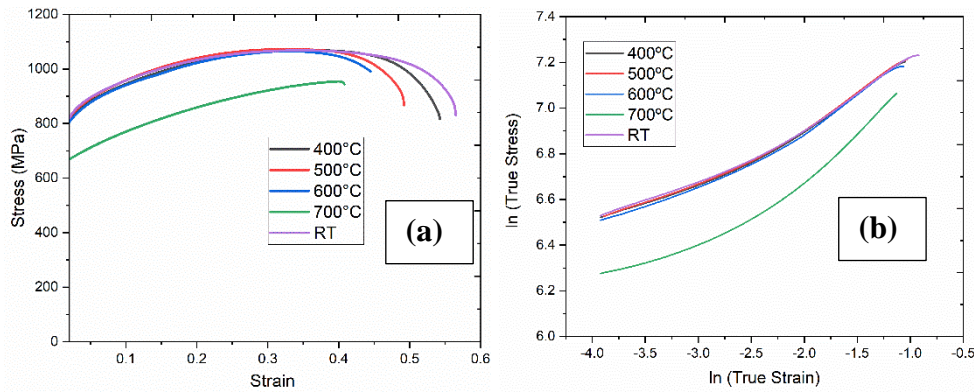
Figure 5.4: Tensile behavior of the Fe-18Cr-21Mn-0.65N austenitic stainless steel, solution treated and pre exposed from 400°C to 700°C for 100 h, and tested at the respective temperature of pre-exposure: (a) engineering stress strain curves and (b) true stress strain plots.

Table 5.2: Tensile properties of the Fe-18Cr-21Mn-0.65N austenitic stainless steel, solution treated and exposed from 400°C to 700°C for 100 h, and tested at the respective temperature of pre-exposure.

Test Temperature (°C)	Yield strength (MPa)	Tensile Strength (MPa)	Elongation (%)
RT	668	918	56
400	663	913	54
500	666	924	49
600	662	854	44
700	479	802	40

Table 5. 3: Bulk hardness of the Fe-18Cr-21Mn-0.65N austenitic stainless-steel specimens of cross section, from the center region at room temperature, solution treated and exposed from 400°C to 700°C for 100 h, eroded at the respective temperature of pre-exposure.

Temperature (°C)	Hardness (Hv)
RT	342±4
400	338±5
500	308±7
600	299±5
700	275±6

Table 5.4: Strain hardening and strength coefficient of the Fe-18Cr-21Mn-0.65N austenitic stainless steel, solution treated and exposed from 400 to 700°C for 100 h and tested at the respective temperature of pre-exposure.

Test Temperature (°C)	n	K (MPa)
RT	0.234±0.001	1885±4
400	0.234±0.002	1871±5
500	0.232±0.003	1871±3
600	0.231±0.001	1842±2
700	0.226±0.002	1688±3

5.2.5 Surface Morphology

Figure 5.5 shows SEM micrographs of scar region of samples of the Fe-18Cr-21Mn-0.65N austenitic stainless steel eroded at RT, 400, 500, 600, and 700℃ at three impact angles of 60̊, 75̊ and 90̊.
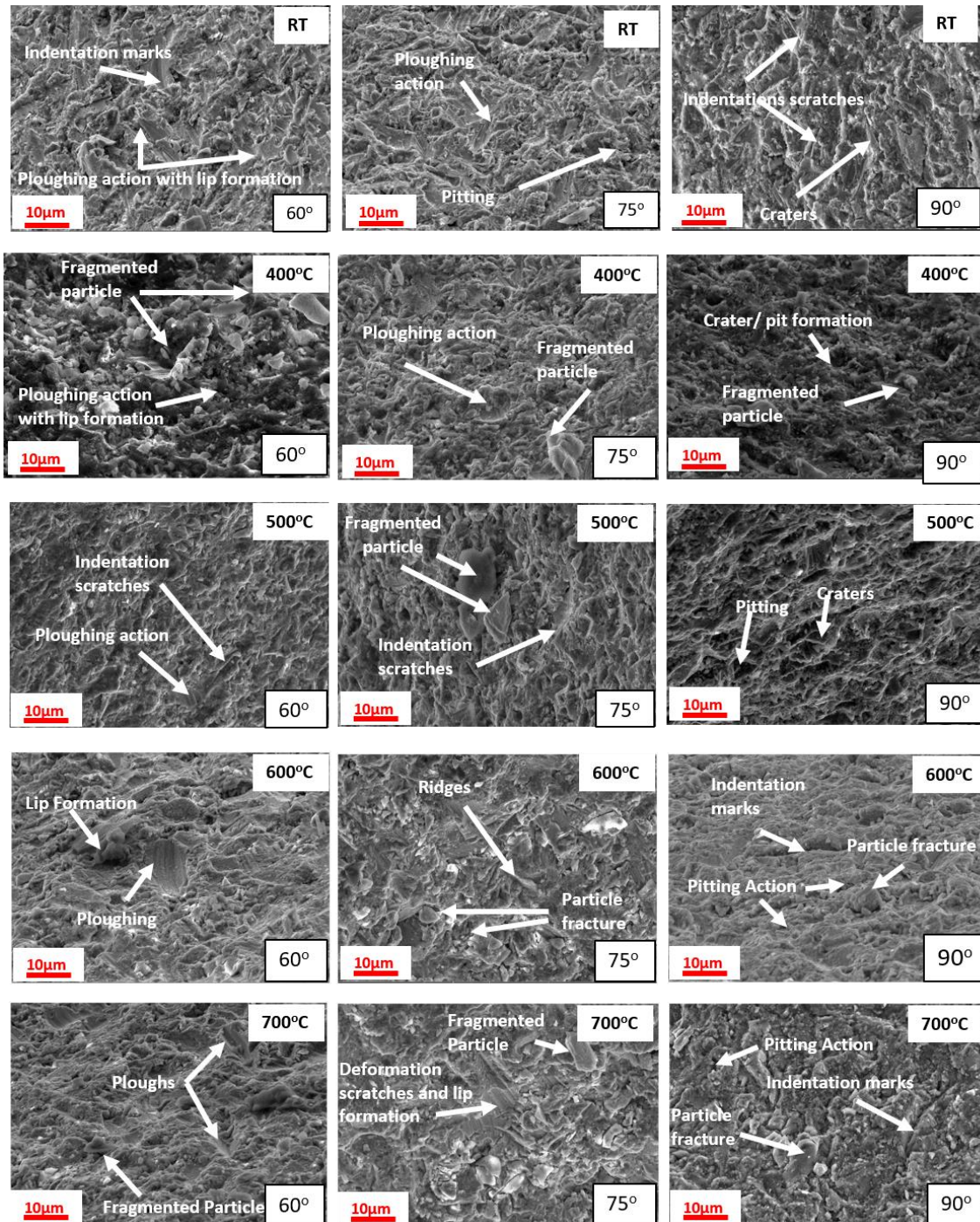

Figure 5.5: SEM micrographs of the areas of the Fe-18Cr-21Mn-0.65N austenitic stainless steel, eroded at: room temperature, 400℃, 500℃, 600℃ and 700℃.

Different artifacts can be seen, which are signature marks of ductile metal cutting. At impact angles of 60°, 75° ploughing and particle fracture is there whereas at 90° of impact angle indention marks with pitting action are observed at the surface. The horizontal and vertical components of velocity caused the particle to penetrate deeper in the metal surface and removal of metal particles by lateral movement respectively. Features such as ploughing/ micro cutting, lip formation, and indentation marks can also be seen. These marks are formed by the impact of high velocity alumina particles on the surface, resulting in ploughing of the material and its accumulation as a result in lip formation. Indentation marks can also be seen on the surface which is result of the hard particle impact. At normal angle, craters formation and pit formation can be seen because only normal component of velocity is available at a normal angle which causes material removal by delamination or excessive deformation. This excessive deformation also causes an increase in the hardness values specially at the subsurface region of the impact, at 90° impingement.

As temperature increased to 400°C, the depth of ploughing increased at 60° and 75° impingement and lips were formed. More fragmented particles can be seen on the surface which shows that the severity of erosion increases with the temperature rise. Fragmented particles can be seen at the surface which get detached from the metal surface due to the subsequent impact of high velocity particles. At a normal angle, craters and pits formation occurred due to the rebound of impinging particles from the surface. At 500°C, the artifacts were of similar intensity as that formed at 400°C but with increase in temperature to 600°C, there was increase in the size of the ploughing mark. The weight loss plots (**Figure 5.1**) show that the erosion rate increases sharply at higher temperatures. The intensity of these artifacts is increased showing higher weight loss at 600°C. At 700°C, deformation scratches and lip formation were the primary modes of material removal, and at 90° of impingement crater formation takes place by removal of metal from the surface. Higher temperature pre-

exposure resulted in decrease in hardness and ductility of material specially at 600 and
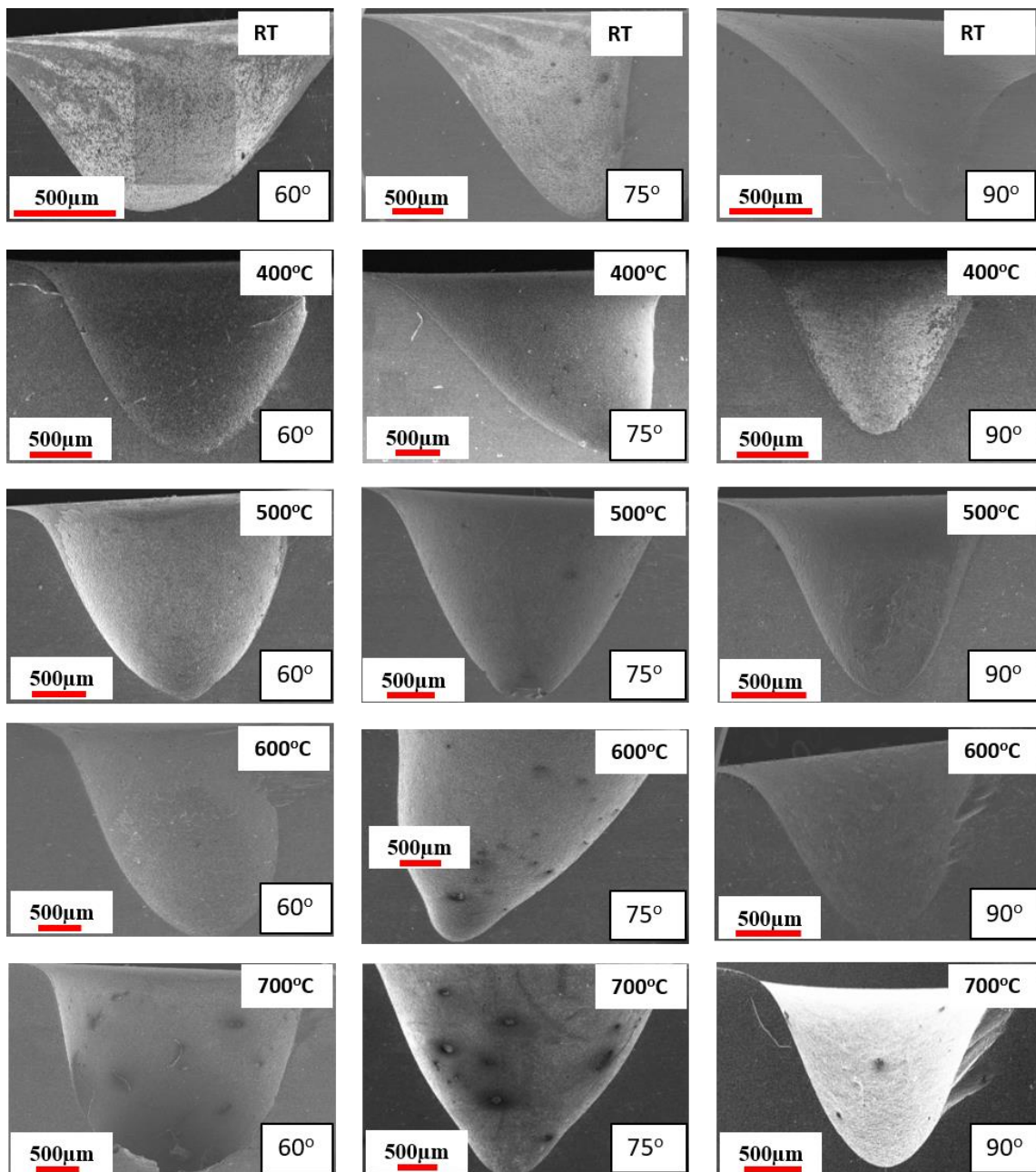
700°C which further enhanced the erosion process.

Figure 5.6: SEM micrographs of cross section of eroded scar showing the eroded crater profile of 18Cr-21Mn-0.65N-Fe austenitic stainless steel at RT, 400°C, 500°C, 600°C and 700°C.

5.2.6 Cross Sectional Analysis

Cross sectional analysis helps in understanding of the underlying mechanism of material

erosion during the impact of high hardness alumina particles. **Figure 5.6** shows surface

profile of eroded scar of the high manganese nitrogen stabilized austenitic stainless steel with variation of the angle of impingement and the temperature of erosion. It shows that the depth and scar area increased with increasing temperature. At a lower angle, the scar area is higher compared to a higher angle of impact in all the cases. Also, the shape of the scar area changes with the angle of impingement at all temperatures. The scar opening at 60° impingement angle was wider compared to other angles. At 75° of impact angle asymmetrical valleys can be seen at room temperature and 400°C, while at 500-700°C, a pen tip shaped erosion profile was observed. At 90° of impingement the depth of erosion scar was less and the opening was narrower compared to those at 60° and 75° impact angles. **Figure 5.7** shows the cross section of eroded scars formed at RT, 400, 500, 600, and 700°C with varying angle. It shows that at room temperature ploughs were present and fragmented particles formed by the impact of high velocity particles. As the angle of impingement increased eroded surfaces were almost free from ploughs and deep craters were observed.

At 400°C, impact of high velocity alumina particle causes craters and lip formation at lower angle of impact whereas with increasing angle of impact, craters and pitting were dominant. As temperature increases, at lower impinging angle of 60° cracks and embedded alumina particles can be seen in **Figure 5.7**. At 500 and 600°C craters and ploughing, marks were deeper at the lower angle of impingement whereas at higher angles shallow craters can be seen. At the normal angle of impingement, crater formation can be seen with a particle entrapped in it and the depth of crater was highest as compared to other exposure temperatures. At 700°C the crack depth was highest which shows the highest rate of erosion at lower angle of impingement. This was related to the drop in hardness and decrease in ductility at 700°C. Lip and ridge formation were the main mechanisms of metal removal at higher angles of impingement.
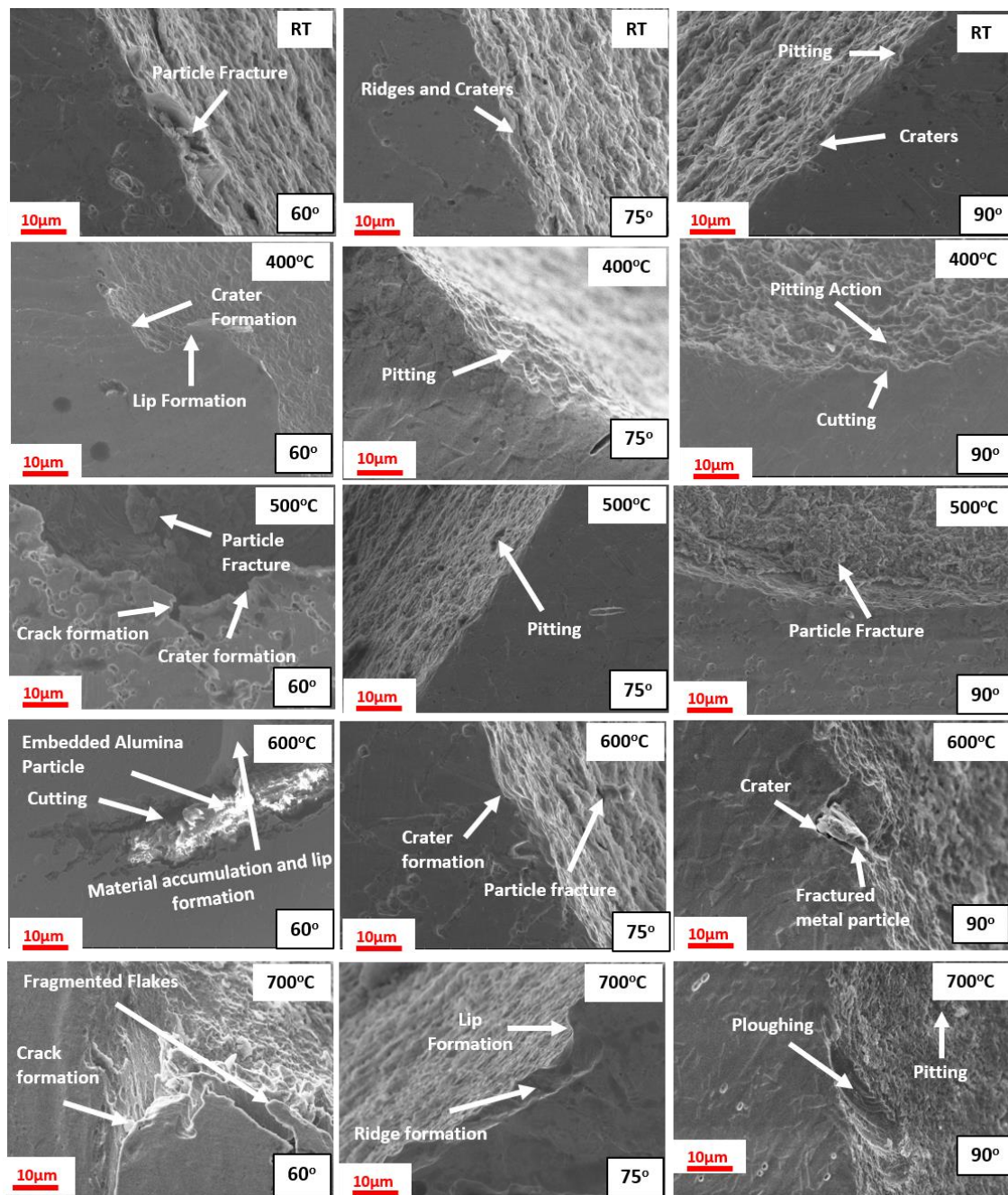
Figure 5.7: SEM micrographs of cross section of areas of the Fe-18Cr-21Mn-0.65N austenitic stainless steel, eroded at: room temperature, 400°C, 500°C, 600°C and 700°C.

5.3. Discussion

Erosion behavior of the high manganese nitrogen stabilized austenitic stainless steel (Fe-18Cr-21Mn-0.65N) was studied, varying the temperature of pre-exposure and conducting erosion tests at the respective temperatures of pre-exposure, at three different angles of impingement. Nitrogen in matrix provides strengthening, improves the tensile properties of steel by electrostatic interaction between dislocations and nitrogen atom compared to other

nickel bearing steels [126-128]. The erosion rate strongly depends upon alloy composition, initial microstructure, exposure temperature, type of erodent's and its impact angle.

5.3.1 Effect of Oxidation

Oxidation behavior of the Fe-18Cr-21Mn-0.65N austenitic stainless steel has been studied by the authors in air from 400 to 700°C up to 100 h. In this study, the alloy showed significant weight gain at 600 and 700°C whereas at 400 and 500°C the weight gain was very less [127]. During erosion at 600 and 700°C, oxidation was prominent which was also observed in Chapter 3. XRD analysis (**Figure 5.8**) of the eroded surface shows the formation of Mn_2O_3 scale and precipitation of Cr_2N. **Figure 5.9** shows a distinct oxide layer composed of spinel of Mn, Cr, and O which shows that manganese and chromium get diffused towards the surface leaving the surface deficient in Mn and Cr. This causes transformation of austenite to ferrite at the surface [129]. The hardness of ferrite formed is lower (~175 H_v) than that of the austenite matrix (308-275 Hv) exposed in the temperature range of 500-700°C [89]. Impingement of high velocity alumina particles and simultaneous transformation of austenite to soft ferrite leads to an abrupt increase in erosion rate at 600 and 700°C.
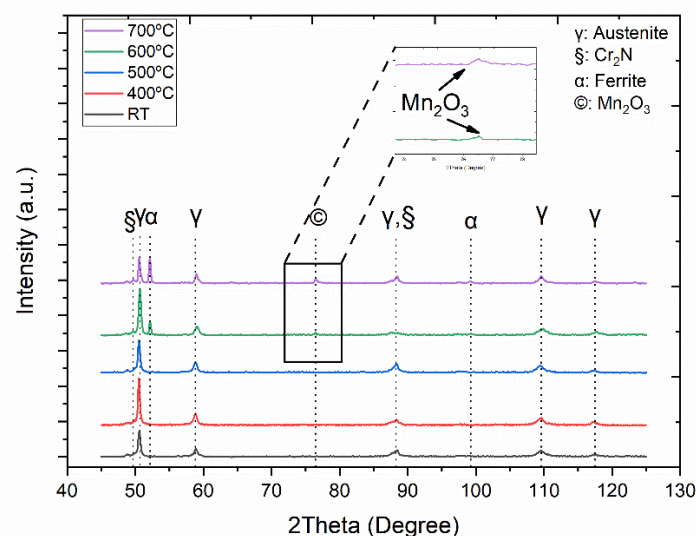

Figure 5.8: XRD pattern of the Fe-18Cr-21Mn-0.65N austenitic stainless steel exposed at different temperature during erosion test.
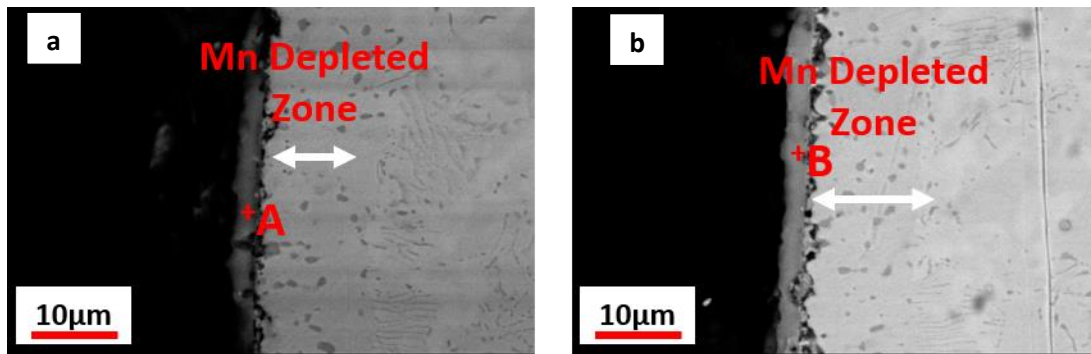
Element	Weight% (A)	Weight% (B)
O K	9.44	16.19
Cr K	13.26	11.33
Mn K	77.30	72.48

Figure 5.9: BSE images of cross section of the Fe-18Cr-21Mn-0.65N austenitic stainless steel pre oxidized for 100 h (a) 600°C and (b) 700°C.

Figure 5.10: Schematic diagrams showing mechanism of erosion of the Fe-18Cr-21Mn-0.65N austenitic stainless steel, at impact angles of (a) 60°, 75°, and (b) 90° at 600 and 700°C.

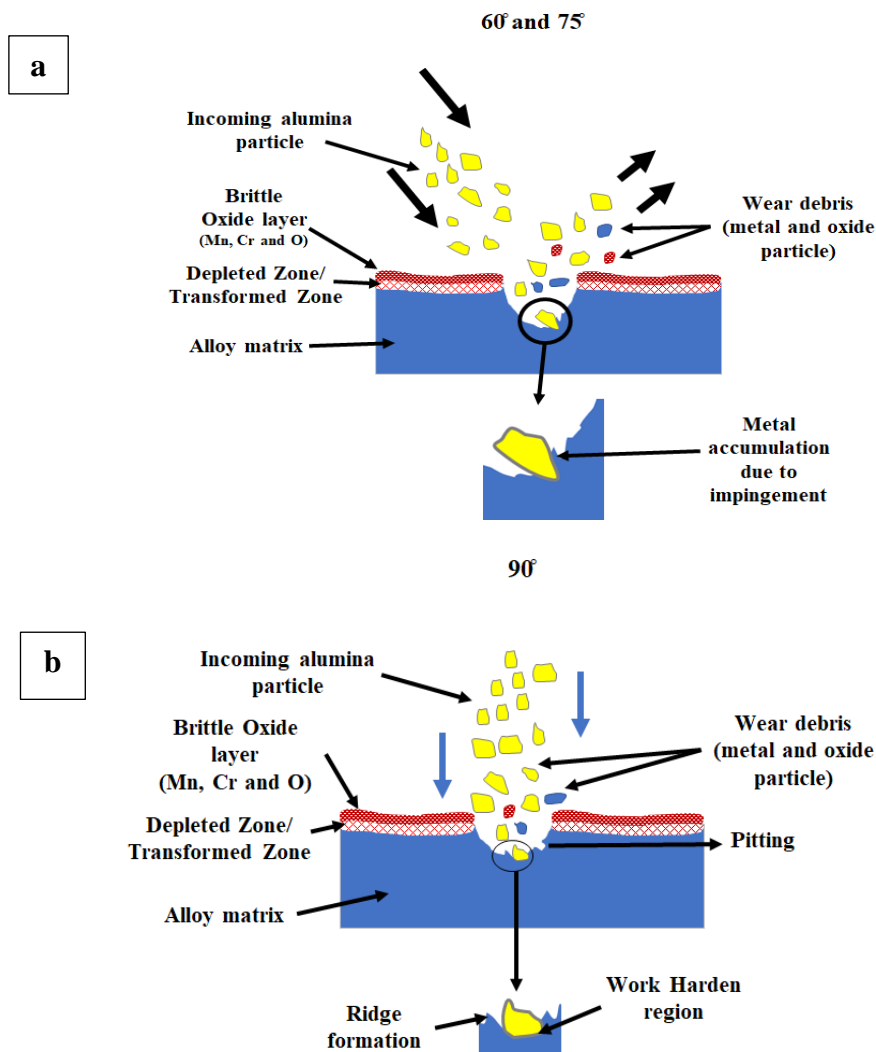Erosion-oxidation synergism is well discussed in the literature [130, 131] and it shows that as temperature increases wastage of material increases. When a high velocity alumina particle impacts the comparatively brittle oxide layer, the surface oxide layer gets detached, and the base material is exposed to the incoming alumina particles, leading to removal of the material. After removal of the preformed oxide layer by the impact of alumina particles, the transformed ferrite region comes directly in contact of erodent particles which is softer than austenite. This transformed region, below the oxide layer, facilitates the process of erosion shown in **Figure 5.10**. It explains the mechanism of erosion at 600 and 700°C on the samples pre oxidized at 600-700°C for 100 h. The uniform and brittle oxide layer does not show any effect on the overall erosion process. The velocity of incoming alumina particles in the present study is too high which does not provide sufficient time for the reoxidation. This causes direct interaction of the bulk material to the incoming alumina particles. In short, pre oxidation at 600-700°C accelerated the metal wastage, compared to that at 400-500°C, due to rapid scaling and microstructural changes near the surface region.

5.3.2 Effect of Temperature

Temperature plays an important role on the erosion rate because it influences the material properties. More precisely it causes microstructural changes which sometimes enhance the erosion rate by increasing the work hardening. Precipitation of nitrides/carbides in stainless steel reduces the capability of the material to work harden. It can be seen from **Figure 5.2 a**, that up to 500°C, erosion rate increases steadily whereas, at 600 and 700°C, it increases sharply. The values of erosion rate at RT, 400 and 500°C were 3.76×10^{-4}, 4.88×10^{-4} and 5.44×10^{-4} respectively, while at 600 and 700°C erosion rates were 6.11×10^{-4} and 7.65×10^{-4} at lower impact angle of 60°. There was a 75% and 100% increase in erosion rate at 600 and 700°C compared to that at room temperature at lower impact angle of 60°. This is related to significant microstructural change at higher temperature of exposure which leads to an

abrupt increase in the erosion rate. In high nitrogen nickel free austenitic stainless steel this problem is more prominent at higher temperatures. Above 500°C, precipitation of harmful chromium nitride starts which causes a decrease in strength and hardness of the material [127]. TEM analysis in the Chapter 1 shows that at a higher temperature of 600 and 700°C precipitation of lamellar chromium nitride takes place after exposure of 100 h [127]. Cr_2N precipitates are brittle in nature and their morphology affects the mechanical properties. Globular and lamellar morphology delays the fracture process but at the same time, the ability of the austenitic matrix to get solid solution strengthened gets reduced. During erosion, these brittle nitrides act as crack initiation sites resulting in fracture of the material.

Strength and ductility both influence the erosion rate. Decrease in the strength and ductility was due to loss in solid solution strengthening. **Figure 5.4a** shows that the ductility and tensile strength fall with increasing temperature of exposure. Table 5.3 shows that the value of work hardening coefficient changes with increasing temperature: at RT and 400°C it was 0.232 but from 500°C it starts decreasing and reaches to 0.226 at 700°C. The pre-exponential coefficient also decreases to 1688 MPa at 700°C from 1885 MPa at RT. This results in decrease in the ability of material to get work hardened and consequent increase in erosion rate at higher temperatures. Decrease of 21% and 29% in ductility at 600 and 700°C respectively compared to room temperature also causes an increase in erosion rate at these temperatures. Foley et al. showed that higher ductility enhances the erosion resistance of a material [132]. Higher ductility facilitates easy dissipation of kinetic energy of the impacting particle by plastic deformation in the localized region of impact. Due to surface deformation, hardness at the surface increases, as shown in **Figure 5.3**. Beneath the deformed surface a cold worked zone was developed resulting in higher hardness. The artifacts generated due to erosion were similar at all the test temperatures but at higher

temperatures, as shown in **Figure 5.5**, ploughs are more elongated and indentation marks are dense.

Various studies on tribological behavior show that stacking fault energy influences the applied mechanism such as ploughing and cutting. It is necessary to understand the effect of alloying elements and exposure temperature both of which influence the stacking fault energy. L. Mosecker et .al.[133] have reported stacking fault energy of various Fe-Cr-Mn-N systems which ranges from 20 to 40 mJ/m^2. They have also reported a linear dependency of stacking fault energy with temperature. As temperature increases stacking fault energy increases which causes the deformation mechanism to change from dislocation glide and mechanical twining to dislocation glide [134]. At room temperature where stacking fault energy is lower, dislocation glide and mechanical twinning are the primary deformation mechanism [135]. Higher stacking fault energy causes reduction in the distance between two partial dislocations and commences easy dislocation glide. With increasing stacking fault energy, material loses its ability to work harden, which increases erosion rate[129]. As discussed here, in the present study phase changes associated with the temperature rise played a very important role in enhancing the erosion rate at 600 to 700°C.

5.3.3 Effect of Impact Angle
Low impact angle (60• and 75•)

Figure 5.10 a explains the probable mechanisms of material removal at lower impingement angles of 60̊ and 75̊. Erosion rate (metal wastage) was higher at the lowest impingement angle of 60°. This is likely to happen when sharp angular particles hits at 100 m/s, the force associated with this impact surpasses the critical force needed for cutting, which results in deep groves and material accumulation at the trailing edge. Further impact on these ridges causes work hardening of ridges which leads to fracture. At lower angle of impact ploughing/cutting was prominent, but as temperature of exposure increases the size of these

artifacts increases. Cutting/ploughing with localized plastic deformation followed by lip formation can also be seen in the present study (**Figure 5.5**). Finnie's and G Sundararajan's model of erosion was followed at lower angle of impingement [136, 137]. At lower angle of impact, the erosion craters are wider because at this angle, area of interaction of impinging particles is more, which causes easy shearing of material. It can be seen from **Figure 5.6** that at lower angle of impact, the scar area is greater than the normal angle of impact. At 75° of impingement, the depth of erosion craters was 2.05, 2.13, 2.17, 2.59 and 2.63 µm at RT, 400, 500, 600 and 700°C respectively.

Table 5.5: Effect of the angle of impact on the depth of erosion scar after erosion at RT, 400, 500, 600 and 700°C.

Angle	Depth (mm) (RT)	Error ±	Depth (mm) (400°C)	Error ±	Depth (mm) (500°C)	Error ±	Depth (mm) (600°C)	Error ±	Depth (mm) (700°C)	Error ±
60°	0.9	0.12	1.54	0.14	1.89	0.10	2.45	0.09	2.51	0.12
75°	2.05	0.16	2.13	0.11	2.17	0.11	2.59	0.12	2.63	0.10
90°	1.18	0.13	1.23	0.10	1.39	0.14	1.48	0.11	1.52	0.23

As shown in Table 5.4, there was not much difference between the scar depths observed at 60° and 75° impact angles except at RT. On unexposed specimens, at 60° angle of impact, the scar depth was only 0.9 mm whereas at 75° angle, it was 2.05 mm. It means 75° impact angle was more damaging compared to other angles of impact. When the impingement angle is closer to normal, the lateral component becomes less active and removal of material due to deeper penetration gives rise to higher depth of scar. **Figure 5.3** shows that the hardness of the subsurface region at an impinging angle of 75° (~375-320 Hv) was marginally higher than that at 60° (~350-290 Hv). This increase in hardness is associated with higher degree of work hardening, at higher angle of impact, at all temperatures of exposure (**Figure 5.4 b** and Table **5.3**).

High Impact Angle (90$^{\bullet}$*)*

At impact angle of 90° to surface of the specimen, delamination and pitting was prominent as shown in **Figure 5.5**. Impact of alumina particle leads to fracture of surface, in form of wear debris. This leads to an increase in the erosion rate initially but repeated impact causes work hardening in the subsurface, below the impact craters. Repeated impact leads to work hardening and subsequent cracks formation causes removal of material. **Figure 5.10 b** shows possible mechanism of material loss at 90° impingement angle. Hardness values (~430-350 Hv) of the subsurface region, below the impact crater, are highest among all the cases, which shows that only horizontal component of velocity causes the higher plastic deformation and lower depth of the scar. At RT, the depth of scar after erosion was 1.18mm, without pre oxidation, which increased maximum up to 1.52 mm at 700°C on pre oxidized samples at 700°C for 100 h. It shows higher erosion resistance of this steel at elevated temperature of exposure at normal angle of impact.

5.4 Comparison with Literature

A comparison of the erosion rate of low-cost nickel free austenitic stainless steel with nickel containing stainless steel shows that nickel free austenitic stainless steel performs better in similar conditions. Table 5.5 presents the rate of erosion of different nickel containing stainless steels, available in literature. A study carried out by H. Nautiyal et. al [138] on high temperature erosive wear of AISI 316 stainless steel, with similar operating parameters, erodent and method, shows that at 400°C the erosion rate at an angle of 60° and 90° was 6.5×10^{-4} and 5.3×10^{-4} respectively whereas at 600°C, it was 7.5×10^{-4} at 60° and 7.4×10^{-4} at 90° respectively. In comparison with this, the erosion rate of high manganese nitrogen stabilized nickel free austenitic stainless steel is 4.8×10^{-4} at 60° and 3.44×10^{-4} at 90°, at 400°C whereas at 600°C, it is 6.6×10^{-4} at 60° and 4.7×10^{-4} at 90° respectively. This can be explained on the basis of higher strength and hardness of high manganese nitrogen

stabilized nickel free austenitic stainless steel [139]. Studies on 316 L SS by Bhosale et al. and A Selokar et al., with less intensive operating parameter (velocity=30 m/sec) compared to present study (velocity= 100m/sec), show that the erosion rate was higher compared to high manganese nitrogen stabilized austenitic stainless steel [123, 139]. 304 austenitic stainless steel shows better performance but the parameters were less extreme compared to the present study [140]. In another study on 304 carried by A. Azad et al [141] with increased velocity and at normal angle of impingement, the erosion rate was higher compared to high manganese nitrogen stabilized austenitic stainless steel.

Table 5.6. Comparison of erosion rate of various nickel containing austenitic stainless steels.

S.No.	Erosion Parameter							Alloy		ER (g/g)	References
	A	*v (m/s)*	*t (min)*	*T (°C)*	*DR (g/min)*	*E*	*ES (µm)*				
1.	60°,90°	41	27	RT	3	S	53-75	316L		5.1×10^{-4} 3.5×10^{-4}	[139]
2.	90°	30	10	500	2	AL	50-70	316L		1.2×10^{-3}	[123]
3.	60°, 90°	24	10	RT	150	S	420-450	304		7.25×10^{-4} at 60° 5.17×10^{-4} at 90°	[142]
								316		5.35×10^{-4} at 60° 4.93×10^{-4} at 90°	
4.	90°	40	5	RT	5	AL	50	304		1.4×10^{-5}	[140].
5.	60°,90°	100	20	400, 600	4.6	AL	50	316	400°C	$\sim 6.5 \times 10^{-4}$ at 60° $\sim 5.3 \times 10^{-4}$ at 90°	[138]
									600°C	$\sim 7.5 \times 10^{-4}$ at 60° $\sim 7.4 \times 10^{-4}$ at 90°	
6.	90°	85	16	RT	6.3	S	50	304		$\sim 3.2 \times 10^{-4}$	[141]

Note: *A= Angle; v= Velocity; t= Time; DR= Discharge Rate; E= Erodent; ES= Erodent Size; T= Temperature; ER= Erosion Rate; RT= Room Temperature; AL=Alumina;*

Mechanical properties such as yield strength, ultimate tensile strength, hardness and ductility of 316L are lower compared to Fe-18Cr-21Mn-0.65N austenitic stainless steel as shown in Table 1.1. Higher mechanical properties of Fe-18Cr-21Mn-0.65 nitrogen

austenitic stainless steel are the main reason for better erosion resistant. Hardness is one important parameter influencing erosion rate, 316L has ~180 H_v and Fe-18Cr-21Mn-0.65N stainless steel has 323 H_v [9,10]. Comparison of erosion rate of less expensive high manganese nitrogen stabilized (Ni-free) austenitic stainless steel with those of expensive nickel containing conventional stainless steel at different impact angles and exposure temperatures, clearly shows that the present alloy performs better and could be replacement of the existing 316L stainless steel.

5.5 Conclusions

High temperature erosive wear behavior of pre oxidized high manganese nitrogen stabilized austenitic stainless steel (Fe-18Cr-21Mn-0.65N) was studied at three different impingement angles of 60°, 75° and 90° at RT to 700°C. Pre-exposure of the steel produced brittle oxide scale composed of spinel of Mn, Cr, and O. High temperature exposure reduced the tensile strength and hardness of the steel due to precipitation of harmful chromium nitrides (Cr_2N). High velocity impact of alumina particles resulted in breakage of brittle oxide layer and directly eroded the base material. Increase in temperature causes an increase in erosion rate at all impingement angles. As the angle of impingement increased from 60° to 90°, the erosion rate decreased. At 600 and 700°C erosion rate increases rapidly due to the formation of soft ferrite at the surface, below the oxide layer. The changes in hardness were highest at 90° of impingement angle at all temperatures and the erosion rate was lowest. It is attributed to higher plastic deformation and the reduced velocity of the incoming particle by rebounding interaction. The mechanism of erosion was ploughing/ cutting, lip formation at lower angle of impingement, and at normal angle, the delamination and crater/ pit formation was a prominent mechanism at all temperatures. The present study also shows that the Fe-18Cr-21Mn-0.65N alloy can replace the expensive nickel containing 316L stainless steel in applications where metal erosion is observed.